



ARTICLE

Numerical Simulation of Urea Based SNCR Process in a Trinal-Sprayed Precalciner

Yu Liu and Hongtao Kao*

College of Materials Science and Engineering, Nanjing Tech University, Nanjing, 211816, China

*Corresponding Author: Hongtao Kao. Email: Kaoht@163.com

Received: 10 June 2020 Accepted: 28 July 2020

ABSTRACT

In order to study the combustion characteristics, NO_x emission and NH₃ slip in a new trinal-sprayed precalciner, the simulations of combustion and aqueous urea solution based selective non-catalytic reduction (SNCR) process were conducted by computational fluid dynamics in this precalciner, the effects of different injection heights, different injection flow rates and stratified injection under different flow rates on SNCR process were studied. The results showed that the flow field was symmetrically distributed in the precalciner, and the flue gas from the rotary kiln formed the recirculation region on both sides of the cone body, which increased the residence time of the solid particles. The temperature was mainly between 1100 K and 1250 K in the middle and upper column of the precalciner, which met the demand of the pulverized coal combustion and raw material decomposition. The concentration of NO at the outlet of the precalciner was 559 ppm, moreover, different injection heights and different injection flow rates had a strong influence on NO_x removal efficiency and NH₃ slip. The aqueous urea solution should be injected at SNCR-1 to prolong the residence time of NH₃, and injection flow rate had an optimal flow rate but not the higher the better. When the injection flow rate under stratified injection was 0.019 kg/s, which could play a better optimization role on NO removal efficiency on the basis of the injection flow rate. In consideration of cost effective, a stratified injection with an injection flow rate of 0.019 kg/s and an injection height of 20 m, 25 m and 30 m was suggested as a compromise of a satisfactory NO_x reduction rates and reasonable NH₃ slip. Under this condition, numerical simulation result showed that NO_x concentration at the outlet of precalciner was 297.27 mg/Nm³ and NH₃ slip was 4.67 mg/Nm³, meeting emission standard.

KEYWORDS

Trinal-sprayed precalciner; selective non-catalytic reduction; aqueous urea solution; NO_x reduction

1 Introduction

The process of cement production is referred to as “two grinding and one calcination”, which includes the grinding of raw meals, the formation of clinker, and the grinding of clinker mixed with other additives, like slag, gypsum and so on. Before fed into the rotary kiln for calcination, the raw materials should be preheated and decomposed by the precalciner. The precalciner, which is used for coal combustion and the



decomposition of calcium carbonate, is another important piece of equipment for cement production. In order to save raw meals and fuel, refuse-derived fuel [1,2] (RDF) and municipal sewage sludge [3,4] are put into the precalciner for cement production. At the same time, a great deal of exhaust gas was produced by fuel combustion, such as NO_x , which damages the environments seriously. NO_x produced by cement production is the third largest source of nitrogen oxide contaminants after power plant and automotive exhaust. To meet increasingly stringent emission standards, selective catalytic reduction [5,6] (SCR) has been widely applied to power plant and automotive exhaust for NO_x reduction. However, in consideration of cost effective, the most popular methods are staged combustion [7,8] and selective non-catalytic reduction (SNCR) [9–12] for reducing NO_x emissions in cement plant recent years. So, understanding the operation condition of the precalciner is essential in order to obtain good denitration efficiency.

The decomposition of calcium carbonate is the main chemical reaction in the precalciner. Temperature is a significant influence factor for the calcination of calcium carbonate according to the reaction (1). When the temperature is above 873 K, calcium carbonate decomposes slowly. With the temperature increases, when the temperature exceeds 1173 K, the decomposition rate of calcium carbonate improves greatly. Otherwise, CO_2 pressure also has a huge impact on CaCO_3 decomposition. Fig. 1 displays the relation between equilibrium CO_2 pressure and temperature on limestone and the curve can be described by the Eq. (2). Here, $P_{\text{CO}_2}^e$ is given in atmospheres (1 atm = 0.101 MPa), and T is given in Kelvin. When the CO_2 partial pressure in the system is lower than the equilibrium CO_2 pressure over CaCO_3 , calcium carbonate begin to decomposes in five steps: a) the process of heat transfer from the gas to the surface of particle, b) the interior of the particle conducts heat to the reaction surface through the calcium oxide layer, c) chemical reactions on the reaction surface, d) the mass transfer of the reaction product carbon dioxide through the oxide layer, e) the mass transfer of calcium carbonate from the particle surface to the atmosphere.

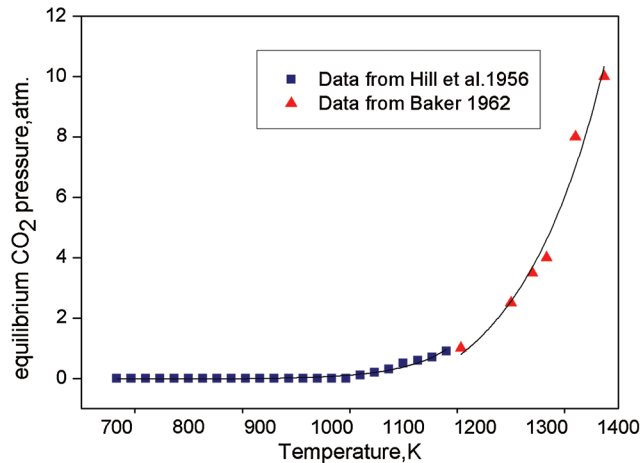


Figure 1: Equilibrium CO_2 pressure over CaCO_3



$$\log_{10} P_{\text{CO}_2}^e = -\frac{8308}{T} + 7.079 \quad (2)$$

The complex flow field is formed in the precalciner due to the interaction of tertiary air and flue gas from the rotary kiln, and the pulverized coal particles and calcium carbonate are in a suspended state. The gas stream formed by tertiary air and flue gas not only affect the trajectory of solid particles but also decide

their residence time. The heat released by coal particles supplies enough energy for the decomposition of the raw meals.

A high calcium carbonate decomposition rate is beneficial to decrease the coal consumption of the rotary kiln so as to reduce the thermal load of the rotary kiln. So, the coal must burn around the calcium carbonate suitably. However, the traditional cold model experiment cannot simulate and predict the complex reacting process. At the same time, NO_x produced by pulverized coal combustion has become an increasingly serious problem in the sustainable development of the cement industry.

In recent years, many scholars and research institutions have conducted a large number of studies on the precalciner from experiments to numerical simulation. According to the research results, the temperature [9,10,13], the gas composition [9,14], CaCO_3 and CaO [15–18] have a different effect on NO_x reduction. In the appropriate temperature window, the higher the temperature, the higher the denitrification efficiency. Moreover, the different gases in the precalciner, like O_2 , CO , H_2 and C_iH_i , also have impact on NO_x reduction. What's more, CaCO_3 and CaO can be used as the catalyst to promote CO to reduce NO_x , but inhibit NO_x reduction by NH_3 , besides experimental studies, numerical simulations of the precalciner were also studied by many scholars and research institutions. Xie et al. [19] used a 3D model for SLC-S precalciner using standard $k - \varepsilon$ model and discrete phase model in order to predict the flow field and particle concentration distribution in the precalciner by adding a raw meal inlet. Huang et al. [20] proposed a new method idea to solve the pole problem of the double-spray precalciner by the RNG (renormalization group) $k - \varepsilon$ model and developed a four-mixture-fraction model to predict the multi-component mutual transportation and the formation of NO in the precalciner. Fidaros et al. [21] studied the relationship between velocity, temperature, gas concentration and particle trajectory in a low NO_x precalciner. Moreover, Computational Fluid Dynamics (CFD) validation studies of combustion characteristics and NO_x emissions based on the actual incinerator had also been published [22], on this basis, the co-combustion characteristics and NO_x emissions in municipal solid waste incinerators with ammonia based SNCR process were studied [11,23]. What's more, reburning zone conditions [24], CaO [25] and different gas compositions [26] on NO_x removal efficiency by selective non-catalytic reduction were explored by CFD software for obtaining the law of NO_x formation in different coal types. In addition, An et al. [27] studied NO_x emission by injecting aqueous urea solution directly based on the 7-step global mechanism. Norbert found that the performance of the 12-step reduced mechanism was better than the 7-step mechanism [28].

In conclusion, it becomes apparent that numerical simulation is important because it not only saves human and material resources but also optimizes operation conditions of precalciner to reduce coal consumption, improve the final cement quality and reduce NO_x emission on the basis of simulation results. Although the above studies had done a great deal of work about different types of precalciner, there is a little research about the newer trinal-sprayed precalciner (TTF) regardless of combustion characteristics or NO_x removal efficiency. Compared with the older precalciner, the newer TTF precalciner has simpler structure, stronger adaptability to fuel, three-sprayed effect, and strong turbulent recirculation, and the feeding modes of pulverized coal and raw material have changed. These unique features make the combustion characteristics in the newer TTF precalciner different from the older precalciner. Therefore, it is significant to analyze the transport of gas-solid two-phase flow in the newer TTF precalciner under cold and hot condition for cement production by numerical simulation. Besides, aqueous urea solution was injected into the precalciner by different injection heights, different injection flow rates and stratified injection under different flow rates to optimize selective non-catalytic reduction process on this basis, which may be beneficial to reduce NO_x emission and provide the groundwork for SNCR process in trinal-sprayed precalciner.

Fig. 2 shows the geometric structure of the trinal-sprayed precalciner. The precalciner is 45.88 m high and is divided into three column sections and one vertebral body section. The three columns are 9.22 m, 12.9 m and 9.1 m from top to bottom, respectively. The cylinder is 7.1 m in diameter and the cone is 5.6 m high. The tertiary air and raw meal duct are symmetrically distributed on both sides of the cylinder at the lower part of the cylinder. The tertiary air enters the horizontal direction tangentially from the lower part of the precalciner column, and the flue gas is sprayed into the precalciner through the shrinkage of the flue chamber, and meets the tertiary air to form a “swirl-spray” effect. The mass fraction of aqueous urea solution is 50% and aqueous urea solution is injected into the precalciner through the SNCR nozzles, which contains three groups and 12 nozzles on the walls and the distribution of each group is shown in Fig. 2B. The heights of low (first), middle (second) and high (third) groups of nozzles are 20 m, 25 m and 30 m, respectively, where we call them SNCR-1, SNCR-2 and SNCR-3, respectively. Fig. 3 is the grid of the precalciner, the precalciner is divided into structured hexahedral structured grid and the number of grids was about 938380. The grids around the coal-injection pipes and raw meals pipes region were encrypted to accommodate the complex structure.

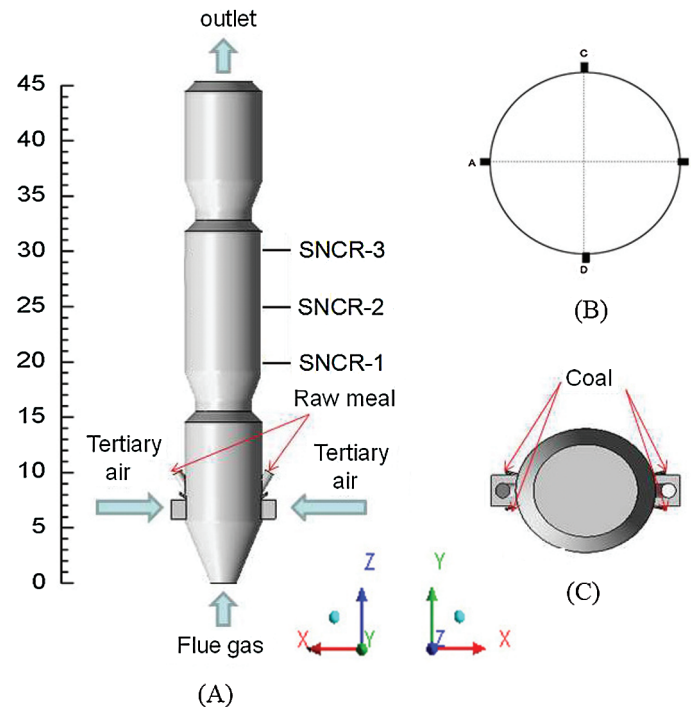


Figure 2: Precalciner structure

2 Mathematical Models

2.1 Fundamental Governing Equation

Computational fluid dynamics is based on the basic governing equations of fluid mechanics including the continuity equation, momentum equation and energy equation. These equations are the three fundamental physical principles that all flows must follow and the corresponding governing equation is as follows:

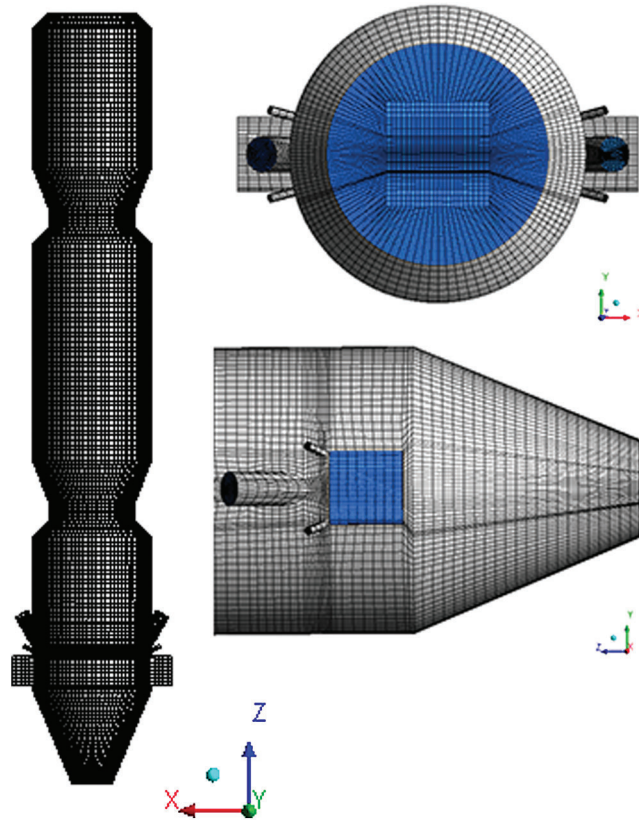


Figure 3: Precalciner mesh

(1) Continuity equation [29]:

$$\frac{\partial \rho}{\partial t} + \left[\frac{\partial(\rho u)}{\partial x} + \frac{\partial(\rho v)}{\partial y} + \frac{\partial(\rho w)}{\partial z} \right] = 0 \tag{3}$$

where ρ is density, t is time, and u, v, w are the components of the velocity vector in the axial, radial, and circumferential directions, respectively.

The Eq. (3), which is in square brackets, is $\nabla \cdot (\rho V)$. So, the Eq. (3) becomes:

$$\frac{\partial \rho}{\partial t} + \nabla \cdot (\rho V) = 0 \tag{4}$$

(2) Momentum equation (Navier-Stokes equation) [29]:

For Newtonian fluids, the Navier-Stokes equation in x, y, z directions is as follows:

$$\frac{\partial(\rho u)}{\partial t} + \nabla \cdot (\rho u V) = -\frac{\partial p}{\partial x} + \frac{\partial \tau_{xx}}{\partial x} + \frac{\partial \tau_{yx}}{\partial y} + \frac{\partial \tau_{zx}}{\partial z} + \rho f_x \tag{5}$$

$$\frac{\partial(\rho v)}{\partial t} + \nabla \cdot (\rho v V) = -\frac{\partial p}{\partial y} + \frac{\partial \tau_{xy}}{\partial x} + \frac{\partial \tau_{yy}}{\partial y} + \frac{\partial \tau_{zy}}{\partial z} + \rho f_y \tag{6}$$

$$\frac{\partial(\rho w)}{\partial t} + \nabla \cdot (\rho w V) = -\frac{\partial p}{\partial z} + \frac{\partial \tau_{xz}}{\partial x} + \frac{\partial \tau_{yz}}{\partial y} + \frac{\partial \tau_{zz}}{\partial z} + \rho f_z \quad (7)$$

where p is pressure, f is volume force on unit mass fluid micelles, and τ is shear stress, which is calculated from:

$$\tau_{xx} = \lambda(\nabla \cdot V) + 2\mu \frac{\partial u}{\partial x} \quad (8)$$

$$\tau_{yy} = \lambda(\nabla \cdot V) + 2\mu \frac{\partial u}{\partial y} \quad (9)$$

$$\tau_{zz} = \lambda(\nabla \cdot V) + 2\mu \frac{\partial u}{\partial z} \quad (10)$$

$$\tau_{xy} = \tau_{yx} = \mu \left(\frac{\partial v}{\partial x} + \frac{\partial u}{\partial y} \right) \quad (11)$$

$$\tau_{xz} = \tau_{zx} = \mu \left(\frac{\partial u}{\partial z} + \frac{\partial w}{\partial x} \right) \quad (12)$$

$$\tau_{yz} = \tau_{zy} = \mu \left(\frac{\partial w}{\partial y} + \frac{\partial v}{\partial z} \right) \quad (13)$$

and μ is the molecular viscosity coefficient and λ is second viscosity coefficient. Stokes made the assumption:

$$\lambda = -\frac{2}{3}\mu \quad (14)$$

(3) Energy equation [29]:

The law of conservation of energy is a fundamental law that a flow system containing heat exchange must follow. The equation is expressed as follows:

$$\frac{\partial(\rho T)}{\partial t} + \frac{\partial(\rho u T)}{\partial x} + \frac{\partial(\rho v T)}{\partial y} + \frac{\partial(\rho w T)}{\partial z} = \frac{\partial}{\partial x} \left(\frac{k}{c_p} \frac{\partial T}{\partial x} \right) + \frac{\partial}{\partial y} \left(\frac{k}{c_p} \frac{\partial T}{\partial y} \right) + \frac{\partial}{\partial z} \left(\frac{k}{c_p} \frac{\partial T}{\partial z} \right) + S_T \quad (15)$$

where T is temperature, c_p is specific heat capacity, k is heat transfer coefficient, and S_T is viscous dissipative term.

2.2 Turbulent Model

Comparing other turbulence models, the $k - \varepsilon$ model is the most widely used model in engineering fluid calculations, including the standard $k - \varepsilon$ model, RNG $k - \varepsilon$ model, and the realizable $k - \varepsilon$ model. Among these models, the realizable $k - \varepsilon$ model is more suitable for simulating the gas flow in the precalciner because of the advantages of simulating jet impact, circular aperture incident flow, secondary recirculation and swirl compared to the other two models.

In the realizable $k - \varepsilon$ model, the transport equation of k and ε is shown as follows [30]:

$$\frac{\partial(\rho k)}{\partial t} + \frac{\partial(\rho k u_i)}{\partial x_i} = \frac{\partial}{\partial x_j} \left[\left(\mu + \frac{\mu_t}{\sigma_k} \right) \frac{\partial k}{\partial x_j} \right] + G_k - \rho \varepsilon \quad (16)$$

$$\frac{\partial(\rho \varepsilon)}{\partial t} + \frac{\partial(\rho \varepsilon u_i)}{\partial x_i} = \frac{\partial}{\partial x_j} \left[\left(\mu + \frac{\mu_t}{\sigma_k} \right) \frac{\partial k}{\partial x_j} \right] + \rho C_1 E \varepsilon - \rho C_2 \frac{\varepsilon^2}{k + \sqrt{\nu \varepsilon}} \quad (17)$$

where

$$\sigma_k = 1.0, \sigma_\varepsilon = 1.2, C_2 = 1.9 \quad (18)$$

$$C_1 = \max\left(0.43, \frac{\eta}{\eta + 0.45}\right) \quad (19)$$

$$\eta = (2E_{ij} \cdot E_{ij})^{1/2} \frac{k}{\varepsilon}, E_{ij} = \frac{1}{2} \left(\frac{\partial u_i}{\partial x_j} + \frac{\partial u_j}{\partial x_i} \right) \quad (20)$$

In these equations, μ represents the viscosity coefficient, E_{ij} is the time-average strain rate. σ_k and σ_ε are the prandtl number corresponding to the turbulent flow energy k and the dissipation rate ε , respectively, G_k is turbulent kinetic energy caused by the average velocity gradient.

2.3 Radiation Model

Considering the characteristics of radiation between the gas phase and the particles, this research adopts the P1 radiation model, which is represented in the following [31]:

$$\nabla \cdot (\Gamma \nabla G) + 4\pi \left[\alpha \frac{\sigma T^4}{\pi} + E_p \right] - [a + a_p] G = 0 \quad (21)$$

where

$$E_p = \lim_{V \rightarrow 0} \sum_{n=1}^N e_{pn} A_{pn} \frac{\sigma T_{pn}^4}{\pi V} \quad (22)$$

$$a_p = \lim_{V \rightarrow 0} \sum_{n=1}^N e_{pn} \frac{A_{pn}}{V} \quad (23)$$

$$\Gamma = \frac{1}{3[\alpha + \alpha_p + \sigma_p]} \quad (24)$$

$$\sigma_p = \lim_{V \rightarrow 0} \sum_{n=1}^N (1 - f_{pn})(1 - e_{pn}) \frac{A_{pn}}{V} \quad (25)$$

2.4 Discrete Phase Model

The physical-chemical process of a series of solid phases in the precalciner, which contains the pulverized coal combustion and the raw material decomposition, is gas-solid interaction in complex field. In this paper, the gas phase and solid phases are identified as the primary phase and the discrete system, respectively. So, the discrete phase model (DPM) [32] is used to simulate the movement of solid particles and the interaction between solid phases and the gas phase.

Because of the strong turbulent motion in the precalciner, the stochastic tracking model was used to simulate the particle dispersion due to turbulence in the fluid phase, the discrete random walk (DRW) model was adopted to account for the turbulence generation or dissipation in the gaseous phase. In addition, considering gravity and drag force, the force balance equation of the particles in three directions in Lagrangian coordinates is as follows:

$$\frac{du_p}{dt} = F_D(u - u_p) + \frac{g_x(\rho_p - \rho)}{\rho_p} \quad (26)$$

$$\frac{dv_p}{dt} = F_D(v - v_p) + \frac{g_y(\rho_p - \rho)}{\rho_p} \quad (27)$$

$$\frac{dw_p}{dt} = F_D(w - w_p) + \frac{g_z(\rho_p - \rho)}{\rho_p} \quad (28)$$

where u_p , v_p and w_p are the velocity components of the particle in the axial, radial, and circumferential directions, respectively, u , v and w are that of the fluid -phase in the axial, radial, and circumferential directions, respectively, and ρ_p and ρ are particle density and fluid particle, respectively. $F_D(u-u_p)$ is the drag force per unit particle mass.

2.5 Pulverized Coal Combustion Model

The pulverized coal particles, when injected into the precalciner, undergo a series of physical-chemical processes including inert heating, water evaporation, devolatilization, char-burning and ash cooling. Among these steps, devolatilization and char-burning are the main processes of coal combustion.

The process of the volatile devolatilization is simulated by the single-kinetic-rate devolatilization model [33], which assumes that the rate of volatilization is a first-order function of the content of volatiles in the particle:

$$-\frac{dm_p}{dt} = A_1 e^{-(E_1/RT)} [(m_p - (1 - f_{v,0})(1 - f_{w,0})m_{p,0})] \quad (29)$$

where m_p and $m_{p,0}$ are particle mass and initial particle mass, respectively, and $f_{v,0}$ and $f_{w,0}$ are the initial mass fraction of the volatiles in the particles and that of the water, respectively.

After the volatiles are released and burned out, the remaining char starts to undergo the surface combustion reaction and the reactionkinetics/finite diffusion rate model was used:

$$-\frac{dm_p}{dt} = -A_p P_{OX} \frac{D_0 K}{D_0 + K} \quad (30)$$

where

$$D_0 = C_1 \frac{[(T_P + T_\infty)/2]^{0.75}}{d_p} \quad (31)$$

$$k = C_2 e^{-(E_2/RT_P)} \quad (32)$$

In these equations, A_p represents particle surface area, P_{ox} is partial pressure of oxygen, T_∞ and T_P are initial particle temperature and the gas temperature around particles, respectively. d_p represents particle diameter following the distribution of Rosin-Rammler and the distribution of particle diameter was shown in [Tab. 1](#).

Table 1: Particle diameter distribution parameters

Size distribution	Minimum size	Median size	Maximum size
diameter	10	42	200

2.6 Chemical Reaction Model

The species transport model was adopted by the reactions involved in the simulation process [34]. In the species transport model, the mass fraction Y_i of the substance is estimated by solving the convection-diffusion equation of the i^{th} substance, and the solution equation can be expressed as:

$$\frac{\partial}{\partial t}(\rho Y_i) + \nabla \cdot (\rho \vec{v} Y_i) = -\nabla \cdot \vec{J}_i + R_i + S_i \quad (33)$$

In this equation, \vec{J}_i is mass diffusion flux caused by concentration gradient, R_i is the net rate of chemical reaction of substance i and S_i is the extra generation rate of discrete phase.

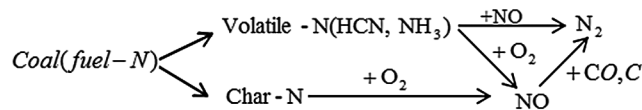
In this paper, the decomposition of raw meals is mainly the decomposition of calcium carbonate (Eq. (1)). The pre-exponential and activation energy of the decomposition reaction of calcium carbonate are $2.47E6 \text{ s}^{-1}$ and 178 kJ/mol , respectively, and the decomposition rate of calcium carbonate is calculated as follows:

$$\alpha = \frac{\text{CaCO}_{3\text{inlet}} - \text{CaCO}_{3\text{outlet}}}{\text{CaCO}_{3\text{inlet}}} * 100\% \quad (34)$$

where $\text{CaCO}_{3\text{inlet}}$ and $\text{CaCO}_{3\text{outlet}}$ are the flow rate of calcium carbonate at the inlet and at the outlet, respectively.

2.7 The Formation of NO_x

The kinetics of fuel NO_x formation is complex, and its reaction mechanism researched by many scholars has not been fully understood. It is generally believed that NO generation is a simple two-step model (Fig. 4).

**Figure 4:** The main reaction path of fuel-N

According to the reaction mechanism, the production rates of HCN and NO can be used as reaction source terms to simulate the generation of NO in the precalciner:

$$S_{HCN} = S_{Volatile \rightarrow HCN} + S_{HCN \rightarrow NO} + S_{HCN \rightarrow N_2} \quad (35)$$

$$S_{NO} = S_{CharN \rightarrow NO} + S_{HCN \rightarrow NO} + S_{NO \xrightarrow{HCN} N_2} + S_{NO \xrightarrow{char} N_2} \quad (36)$$

2.8 SNCR Model

Aqueous urea solution, which is injected into the precalciner through different nozzles, is used as reducing agent to reduce NO_x in this article. The injection type of aqueous urea solution is cone pattern. The non-uniform droplet size distribution is carried out in simulation, which meets the Rosin-Rammler distribution, meanwhile, the motion of the droplet particles are calculated by the Lagrangian formulation

and the interaction of the liquid solutions and the gas phases is introduced through particle sources of Eulerian gas-phase equations. What's more, the dispersion of particles due to turbulence in the fluid phase was considered. Because the temperature in the precalciner is far below the formation temperature of thermal-NO_x, only fuel-NO_x is considered in this article.

We assume that one droplet is formed by a single urea particle. Water evaporates before urea begins its subliming process. The temperature of the injected droplets is controlled by both the convective and radiative heat transfer with the flue gases and the transfer coupled with the latent heat of vaporization. Below the boiling point, the vaporization rate is controlled by convection and diffusion according to the Eq. (37) [35].

$$\frac{dm}{dt} = Sh \cdot D \cdot \pi \cdot d \cdot \rho_{fg} \cdot \ln\left(\frac{1 - y_{vap,fg}}{1 - y_{vap,surf}}\right) \quad (37)$$

where Sh is the Sherwood number, D is dynamic diffusivity, d is droplet diameter, ρ_{fg} is flue gas density, $y_{vap,fg}$ and $y_{vap,surf}$ are vapor mass fraction at the surface and surrounding fluid, respectively. The concentration of vapor at the droplet surface is evaluated by assuming that the partial pressure of vapor at the interface is equal to the saturated vapor pressure, at the particle droplet temperature.

When the particle reaches the boiling temperature (vapor pressure becomes higher than gaseous pressure), the mass transfer is determined by the latent heat of vaporization. Assuming constant droplet temperature during boiling:

$$\frac{dm}{dt} = -\frac{Q_{convection} + Q_{radiation}}{h_{latent}} \quad (38)$$

where Q is the convective and radiative heat transfer, h_{latent} is latent heat of evaporation.

The reactions between NH₃ and NO are used Brouwer's seven-step mechanism (Tab. 2). Brouwer assumed that the breakdown of urea is instantaneous and 1 mole of urea is assumed to produce 1.1 moles of NH₃ and 0.9 moles of HNCO.

Table 2: Seven-step reduced mechanism for SNCR with urea

Reaction	A	b	E
NH ₃ + NO = N ₂ + H ₂ O + H	4.24E + 02	5.30	349937.06
NH ₃ + O ₂ = NO + H ₂ O + H	3.50E - 01	7.65	542284.005
HCNO + M = H + HCNO + M	2.40E + 08	0.85	284637.8
NCO + NO = N ₂ O + CO	1.0E + 07	0.00	-1632.4815
NCO + OH = NO + CO + H	1.0E + 07	0.00	0
N ₂ O + OH = N ₂ + O ₂ + H	2.0E + 06	0.00	41858.5
N ₂ O + M = N ₂ + O + M	6.9E + 17	-2.5	271075.646

2.9 Computational Conditions

The study of SNCR process is consist of three main parts, different injection heights, different injection flow rates and stratified injection under different flow rates on NO_x removal efficiency were explored.

Tab. 3 shows the SNCR operating conditions. In this SNCR process, 0.019 kg/s corresponded to normalized stoichiometric ratios (NSR) and all injection speeds were kept constant at 25 m/s. In the first part, the effect of injection heights on NO_x removal efficiency was explored, in general, NO_x removal

efficiency is closely related to temperature, and the temperature of the precalciner are different in different height. So, this part of the study focused on exploring the effect of heights on NO_x removal efficiency. The aqueous urea solution was injected through SNCR-1, SNCR-2 and SNCR-3 at 0.019 kg/s, respectively. In the second part, the effect of injection flow rates on NO_x reduction was explored, injection flow rates of the aqueous urea solution would affect the production of ammonia, thereby influencing the efficiency of denitrification. So, this part of the study focused on exploring the effect of NSR on NO_x reduction with a ratio of the gradient of 0.2, and the total flow rate was tested at 0.019 kg/s, 0.0228 kg/s, 0.0266 kg/s, 0.0304 kg/s, 0.0342 kg/s and 0.038 kg/s. In the third part, on the basis of the second part, urea solution was injected through SNCR-1, SNCR-2 and SNCR-3 by the fixed ratio to study the effect of the stratified injection on NO_x removal efficiency, and the injection ratio of SNCR-1, SNCR-2 and SNCR-3 was 7:2:1.

Table 3: The SNCR operating conditions

Case	SNCR-1/(kg/s)	SNCR-2/(kg/s)	SNCR-3/(kg/s)	Total flow rate/(kg/s)
0	0.019	0	0	0.019
1	0	0.019	0	0.019
2	0	0	0.019	0.019
3	0.0228	0	0	0.0228
4	0.0266	0	0	0.0266
5	0.0304	0	0	0.0304
6	0.0342	0	0	0.0342
7	0.038	0	0	0.038
8	0.0133	0.0038	0.0019	0.019
9	0.01596	0.00456	0.00228	0.0228
10	0.01862	0.00532	0.00266	0.0266
11	0.02128	0.00608	0.00304	0.0304
12	0.02394	0.00684	0.00342	0.0342
13	0.0266	0.0076	0.0038	0.038

2.10 Numerical Algorithms

The mesh-independent verification of the computational grid is important factors affecting the accuracy of simulation, because this paper focused on the reduction of NO_x emission by SNCR denitration technology, the variation of temperature, O_2 concentration and NO_x concentration of the precalciner outlet was selected for the mesh-independent verification. Five mesh numbers (614,256 cells, 845,568 cells, 938,380 cells, 1,201,054 cells, 1,434,456 cells,) were simulated to record the changes of temperature, O_2 concentration and NO_x concentration of the precalciner outlet. As shown in Tab. 4, a mesh dependency test was performed to determine the appropriate mesh number. The results showed that the mesh used in this study (938,380 cells) was mesh-independent.

Boundary conditions are also important factors affecting the accuracy of simulation. The measured operating conditions of the precalciner are presented in Tabs. 5–7. In addition to calcium carbonate, raw materials also contain clay, sand and other substances, and because calcium carbonate accounts for a large proportion of raw materials, the decomposition of calcium carbonate is mainly used by most scholars [17–19] for the decomposition reaction of raw meals. So all raw meals were simplified to

calcium carbonate in this article. The bituminous coal and the raw meals come from Weinan County of shaanxi Province and Weihui County of Henan Province, respectively. In this simulation, the fixed non-slip state and reflection condition were applied on the surfaces of walls, and the wall is insulated for heat exchange. The outlet value is set as the pressure outlet, given the gauge pressure value -1000 Pa. The pressure-based solver was used for numerical simulation through ANSYS FLUENT, and the pressure velocity coupling was applied to the spatial discretization of SIMPLE algorithm equation using the first-order upwind format.

Table 4: Mesh-independent verification

Mesh number	Parameters		
	Temperature (K)	O ₂ mole fraction (%)	NO (ppm)
614,256	1062.98	3.45	528
845,568	1085.64	3.78	545
938,380	1100.21	4.01	559
1,201,054	1102.05	4.05	561
1,434,456	1099.54	4.03	560

Table 5: Proximate analysis and ultimate analysis of shaanxi bituminous coal

Proximate analysis (%)	Moisture	Volatile matter	Ash	Carbon	Specific energy (MJ/kg)
	2.5	27.46	18.47	51.57	25.29
Ultimate analysis (%)	Carbon	Hydrogen	Oxygen	Nitrogen	Sulfur
	81	7.6	10	1.5	0.7

Table 6: Raw materials compositions (%)

Loss	SiO ₂	Al ₂ O ₃	Fe ₂ O ₃	CaO	MgO
32.47	13.84	3.47	1.87	42.77	1.82

Table 7: Boundary condition of the inlet

	Exhaust gas	Tertiary air	CaCO ₃	Coal
Velocity (m/s)	25	24	3	13
Hydraulic diameter (m)	2.4	3.6	0.85	0.2
Mass flow rate (kg/s)			37.91	1.25
Temperature (K)	1400	1120	1040	331

3 Result and Discussion

3.1 Cold Flow Field

Figs. 5 and 6 show the profiles of velocity, vector and local zoom. From the Figs. 5 and 6, it can be observed that the velocity fields were all symmetrically distributed. The direction of the lower cone speed was dominated by the rising flue gas from the rotary kiln, forming a spray shape. The formation of the recirculation region (① and ②) on both sides of the cone body increased the residence time of the gas and the particles and facilitated heat exchange and decomposition between the raw meals and the gas. Because the tertiary air changed the flow direction of the rising flue gas such that the gas was cut off, the speed reached the minimum at the intersection of the tertiary air and the flue gas from the rotary kiln, and the first sprayed effect was formed. Subsequently, the gas continued to rise through the lower constriction and the upper constriction, respectively, forming the second and third sprayed effect. With the existence of the sprayed region, the pulverized coal particle and raw meal were in suspended condition and fully exchange heat with the flue gas.

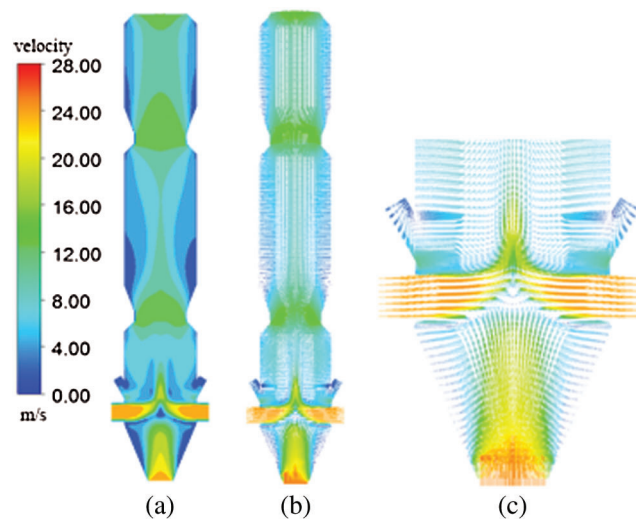


Figure 5: The profiles of velocity, vector and local zoom at $x=0$. (a) Contour, (b) Vector and (c) Zoom

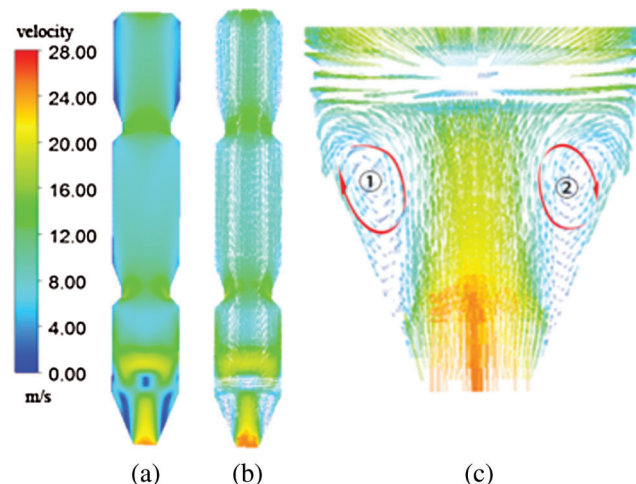


Figure 6: The profiles of velocity, vector and local zoom at $y=0$. (a) Contour, (b) Vector and (c) Zoom

Fig. 7 displays the average velocity along the z direction. From Fig. 7, it can be seen that the maximum average velocity in the precalciner was at the inlet of the flue gas. When the flue gas entered the precalciner at the height of 5 m, the average velocity in the precalciner decreased rapidly. Then, the average flow velocity underwent four increased. The increase of first three average flow velocities, which was caused by the three sprayed effect in the precalciner, was firstly increased and then rapidly decreased at heights of 5 m~7 m, 13 m~17 m and 32 m~34 m, respectively. The fourth increase of average flow velocity was the reason for the decrease of the diameter of the outlet.

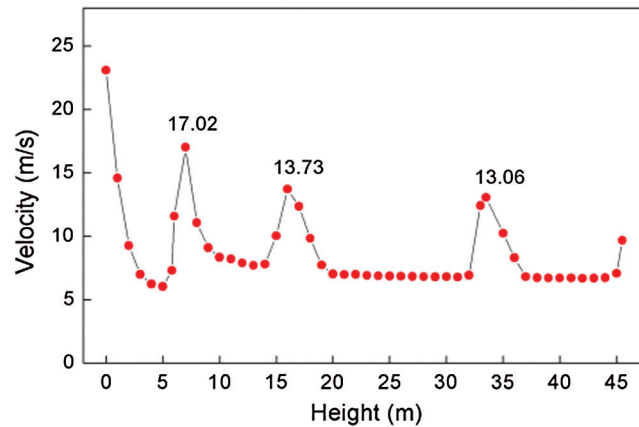


Figure 7: Average velocity along the z direction

Fig. 8 displays the motion path of the gas, the tertiary air and the mixing gas. It can be seen that the dominant motion form of the gas in the precalciner was jet rising flow, and the gas rose vertically along the z-axis in the center of the precalciner. Due to the interaction between the tertiary air and the flue gas, the streamlines on both sides were disordered, and some vortices and swirls appeared near the wall of the precalciner. The simulation result of the average residence time of the gas phase in the precalciner was about 5 s, which is very close to actual design parameters (4.8 s). There is no significant difference between the two results, indicating the reliability of the simulation result.

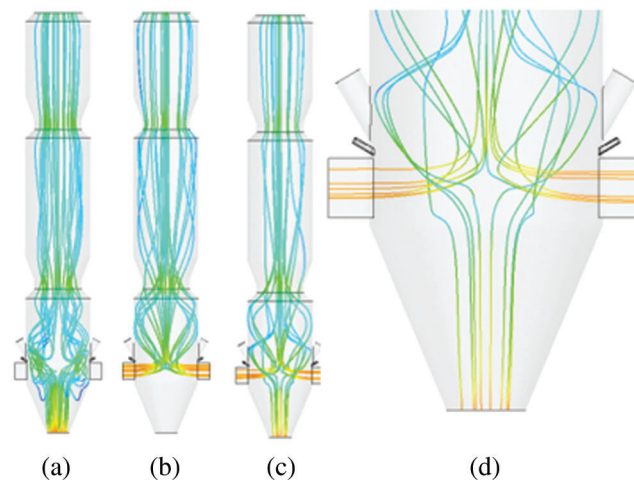


Figure 8: Motion path of the gas, the tertiary air and the mixing. (a) Flue gas (b) Tertiary air (c) Mixing gas and (d) Zoom

3.2 Hot Flow Field

Pulverized coal combustion and calcium carbonate decomposition occurred almost simultaneously in the precalciner, to reveal the complex thermal process. The coupling of coal combustion and CaCO_3 decomposition was simulated. Fig. 9 presents the contours of temperature. It can be observed that there were two high temperature regions in the precalciner. The first region was in the lower part of the cone resulting in the high temperature of the flue gas from the rotary kiln, and the other was in pulverized coal main combustion area due to the heat generation of coal combustion instantly. After that, the temperature decreased slightly and was between 1100 K and 1250 K.

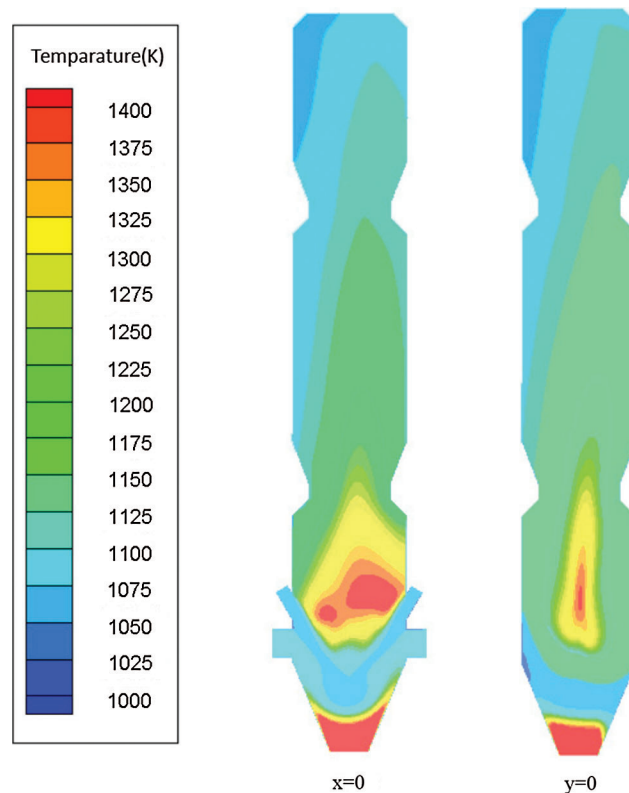


Figure 9: Contours of temperature

In this article, in order to simplifying the model, the decomposition of the CaCO_3 is considered to be the only decomposition reaction. Fig. 10 shows the simulation result of the contours of the mass fraction of CaCO_3 and CaO . Overall, we can see that the mass fraction of CaCO_3 dropped gradually along with the height of the precalciner, but the mass fraction of calcium oxide increased remarkably, which indicates that the calcium carbonate converted to calcium oxide by absorbing the heat of coal combustion. Locally, calcium carbonate decomposition is mainly concentrated in the middle and lower column section of the precalciner, and the decomposition rate of calcium carbonate decreased in the upper cylinder of the precalciner. Finally, almost all the of calcium carbonate decomposed into calcium oxide, and only a small amount of unreacted calcium carbonate escaped from the outlet. According to the simulation result, the flow rate of calcium carbonate at the outlet is 7.19 kg/s, so the decomposition rate of CaCO_3 was 90.51% calculated by Eq. (34), which corresponded to actual measured result [24,36].

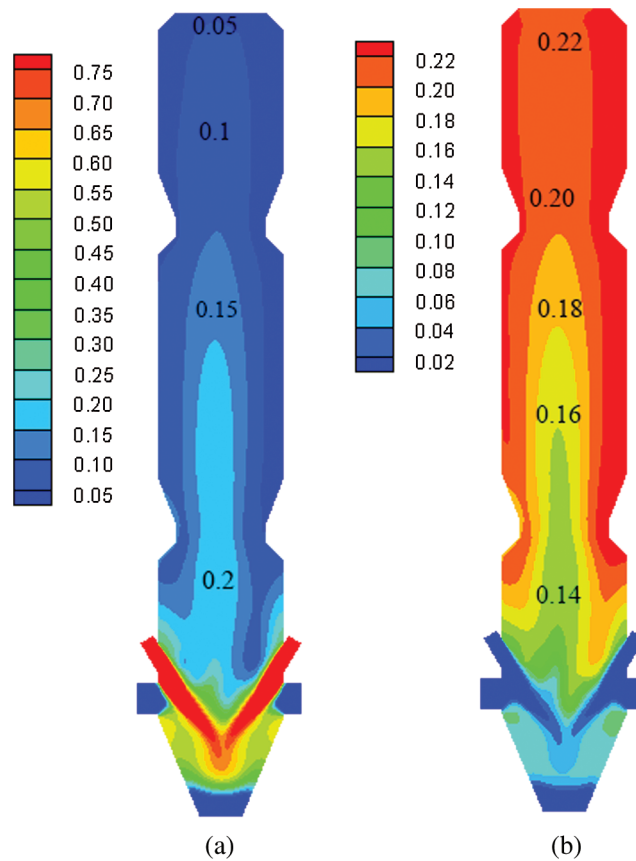


Figure 10: Contours of the mass fraction of (a) CaCO₃ and (b) CaO

The distributions of the average gas temperature and concentrations along the z direction are displayed in Fig. 11. It can be observed that when $z < 7$ m, the temperature decreased rapidly because the calcium carbonate was decomposed into calcium oxide by absorbing the heat. The temperature and CO₂ concentration, with the value at $z = 7$ m, reached the minimum on account of the tertiary air. On the contrary, the mole fraction of O₂ reached the maximum. When $7 \text{ m} < z < 12$ m, the temperature and CO₂ concentration increased sharply due to large quantities of heat and CO₂ produced by coal combustion. At the same time, O₂ concentration decreased rapidly because of O₂ consumed by coal combustion. When $z > 12$ m, the gas temperature and O₂ concentration started to decrease smoothly. This is because the rest of the calcium carbonate continued to decompose by absorbing the heating from the high-temperature gas and the remaining coke continued to burn. According to the simulation result, the temperature at the outlet of the precalciner was 1113 K, which was close to the online measurement value of 1128 K. Moreover, CO₂ concentration continued to increase slowly because of calcium carbonate decomposition. In a word, when $20 \text{ m} < z < 30$ m, the gas concentrations were relatively stable and the temperature was in the SNCR temperature window. In addition, compared with the lower column of the precalciner, the gas flow in the middle column of the precalciner is also more stable (Fig. 8), which was more suitable for the injection of urea solution, so SNCR nozzles should be designed in this position.

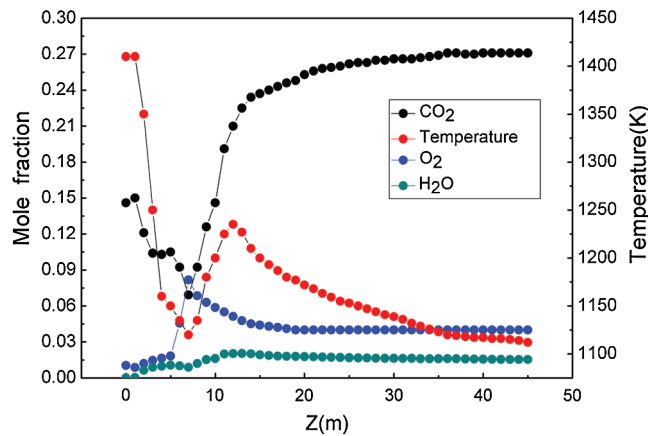


Figure 11: The distributions of the average gas temperature and concentrations along the z direction

3.3 Formation and Analysis of Nitric Oxide

NO_x concentration was affected by two factors in the precalciner, containing fuel-NO_x produced by coal combustion and thermal-NO_x from the rotary kiln. According to the on-line measurements, NO_x concentration from the rotary kiln is about 750 ppm. The contours of NO are shown in Fig. 12. It could be observed that the concentration of NO, appearing at the bottom of the precalciner, was the highest, which could be attributed to the thermal-NO_x produced in the rotary kiln. The lower part of the cylinder at x = 0, a small area with very low NO content was formed near the tertiary air because of the tertiary air without NO, and the concentration of NO in the center of the precalciner and near the wall were about 400 ppm and 500 ppm, respectively. The lower part of the cylinder at y = 0, the lowest and the highest concentration of NO were about 300 ppm and 450 ppm, respectively.

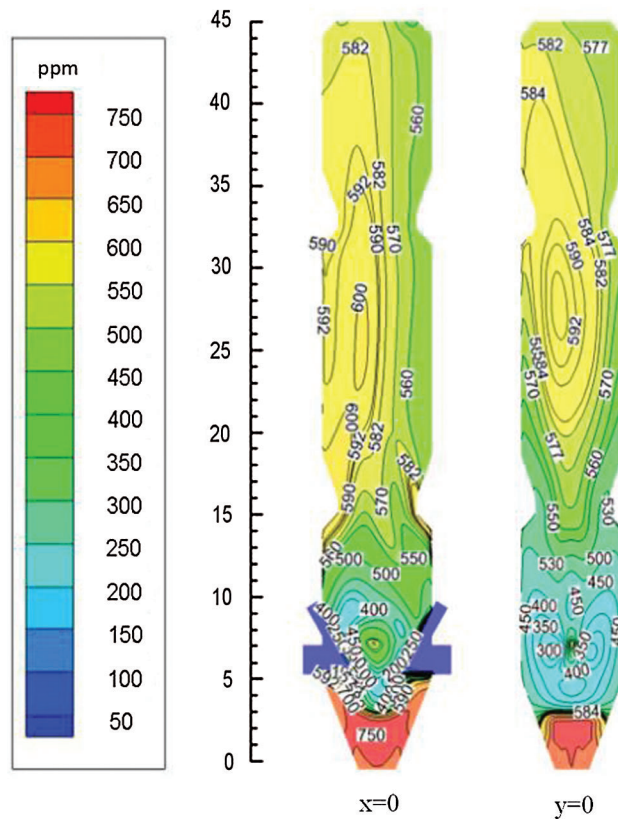


Figure 12: Contours of NO

Fig. 13 showed the average NO concentration along the z direction, it can be observed that when $z < 7$ m, NO concentration in the precalciner dropped rapidly, which is attributed to the dilution effect of tertiary air and the reduction of NO by CO produced by incomplete combustion of pulverized coal. When $7 \text{ m} < z < 12$ m, due to sufficient oxygen in the precalciner, pulverized coal particles burned violently, meanwhile, fuel-N was oxidized completely to form NO rapidly. When $z > 14$ m, because most pulverized coal particles have burned completely, the concentration of NO was stable gradually and NO concentration at the outlet was 559 ppm, which was close to the online measurement value of 615 ppm.

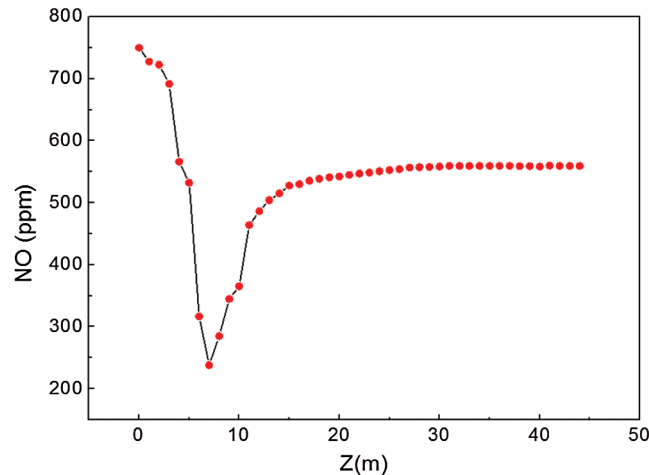


Figure 13: The average NO concentration along the z direction

3.4 Analysis of SNCR Process under Different Injection Conditions

3.4.1 Effects of Different Injection Heights

The contours of NO concentration and NH_3 concentration under different injection heights are displayed in Figs. 14 and 15, respectively. Furthermore, the NO and NH_3 concentrations at the outlet under different injection heights are shown in Fig. 16.

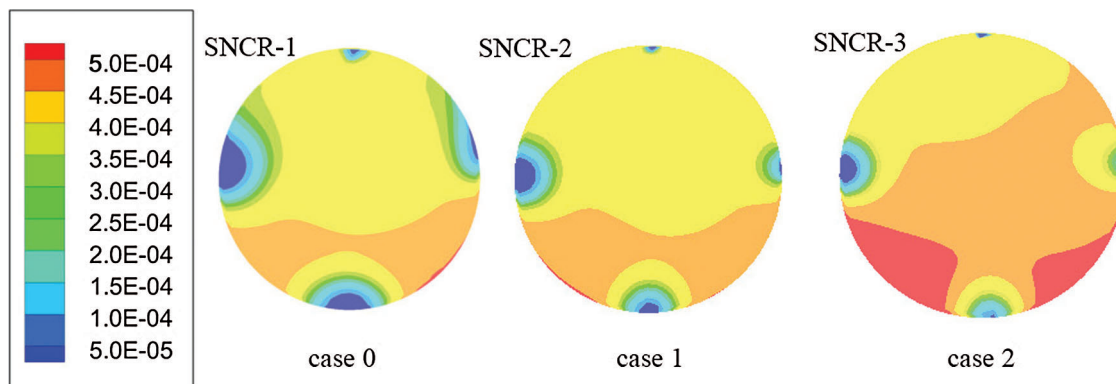


Figure 14: The contours of NO concentration in the precalciner under different injection heights

It can be seen from the Figs. 14 and 15 that the distributions of NO and NH_3 were similar for different cases, which could be attributed to the fact that, when urea was injected into the precalciner, the NH_3 formed at high temperature reacted with NO and O_2 , especially in the four injection locations, a large amount of NO

was reduced to form N_2 . The difference was that the NO concentration in case 2 was the highest, and the NO concentration in case 0 is the lowest, the following reason could explain this phenomena, the average temperature at case 0 is higher than case 2 (Fig. 11) and was more suitable for SNCR reaction. Moreover, the distributions of NO for different cases were uneven, which could attribute to uneven temperature distribution (Fig. 9), the higher the temperature, the more complete the reaction between NH_3 and NO, and the less NO content at the corresponding SNCR injection position. As shown in Fig. 15, NH_3 concentration in case 0 was the highest and NH_3 concentration in case 2 was the lowest for the three cases. This is also because urea pyrolysis is more complete and more NH_3 was formed at high temperature. In addition, NH_3 was only monitored near the four injection positions, and there was almost no NH_3 elsewhere, which indicated that NH_3 reacted completely with NO. The average NO concentration under different injection heights along the z direction is displayed. As can be seen from the Fig. 17, when the aqueous urea solution was injected, a large amount of NH_3 reacted with NO, causing the concentration of NO to dropped sharply first, then a small amount of NH_3 remaining continued to rise and reacted with NO in the precalciner, and the downward trend of NO concentration slowed down. According the simulation results, NO concentrations at the outlet were between 304.28 mg/Nm^3 and 328.84 mg/Nm^3 , which meet the NOx emission standard (400 mg/Nm^3). Moreover, the higher the injection heights, the higher NH_3 slips, but all NH_3 slips were less than 10 mg/Nm^3 , which were lower than the NH_3 emission standard.

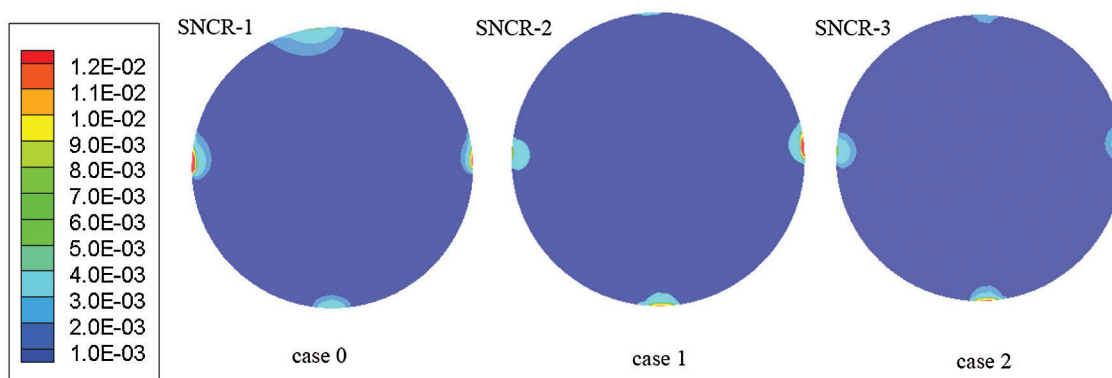


Figure 15: The contours of NH_3 concentration in the precalciner under different injection heights

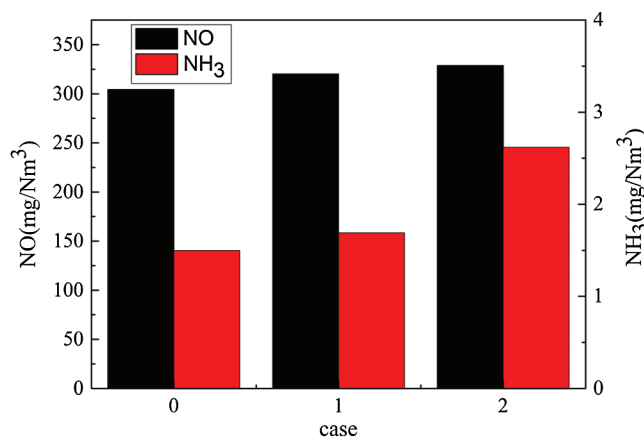


Figure 16: NO and NH_3 concentration at the outlet under different injection heights

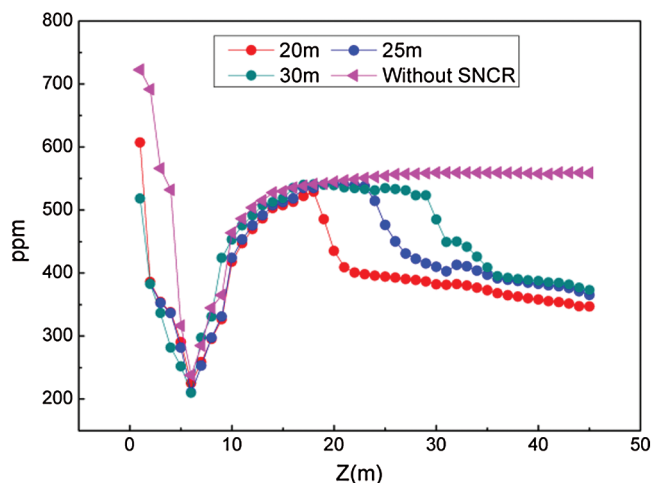


Figure 17: The average NO concentration under different injection heights along the z direction

3.4.2 Effects of Different Flow Rates

The contours of NO concentration and NH_3 concentration under different flow rates are displayed in Figs. 18 and 19, respectively, and the average NO concentration under different flow rates along the z direction is shown in Fig. 20. Moreover, NO and NH_3 concentrations at the outlet under different flow rates are shown in Fig. 21.

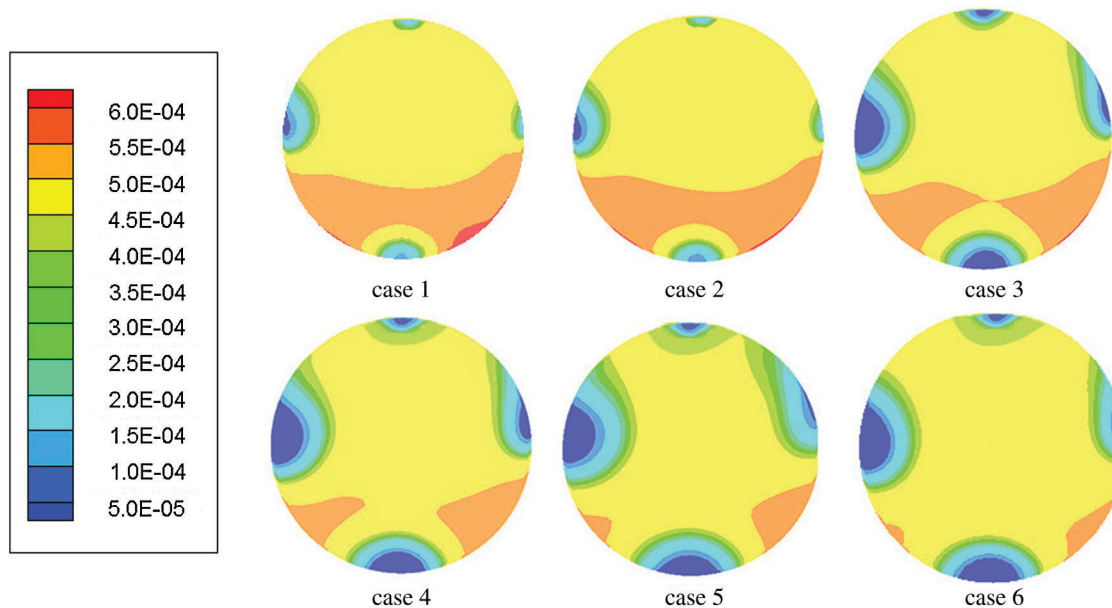


Figure 18: The contours of NO concentration in the precalciner under different flow rates at SNCR-1

As can be seen from Figs. 18 and 20, as the flow rate increased, the NO concentration gradually decreased and the distribution of NO became more uniform. This is because with the increase of urea, more NH_3 produced by the decomposition of urea reacted with NO, which increased NO_x removal efficiency and resulted in a more uniform distribution of NO on the cross section. As shown in Fig. 19, the distribution of NH_3 was similar to the Fig. 15, that is, the high concentrations of NH_3 were only detected at the four injection locations and the other regions was almost

zero, which also proved that the reaction between NH_3 and NO was complete. With the flow rate increased, NH_3 concentration increased slightly at SNCR-1, but the increase was not obvious, at this situation, on the one hand, the NH_3 generated by urea pyrolysis was largely consumed by NO reaction, moreover, although the decomposition of urea was instantaneous. It could be seen from the Fig. 20 that the rapid descent stage of NO after urea injection was 20 m~22 m, which was mainly affected by the upward gas flows in the precalciner, leading to the rise of unreacted NH_3 along with the airflow. These dual function caused NH_3 concentration was not high at SNCR-1. According to the simulation results, the NO concentrations at the outlet were $226.24 \text{ mg/Nm}^3 \sim 297.27 \text{ mg/Nm}^3$, and the reduction efficiency were 37.92% to 54.74%. In addition, the NSR increased by 0.2 every time, the NO concentration decreased by 21.92 mg/Nm^3 , 16.61 mg/Nm^3 , 21.92 mg/Nm^3 , 18.84 mg/Nm^3 and 3.51 mg/Nm^3 , respectively. It can be seen that when NSR was greater than 1.8, the effect of flow rates on NO removal efficiency was small, and NH_3 slip exceeded emission standards (10 mg/Nm^3). So the SNCR injection flow rates had an optimal flow rate but not the higher the better. Results showed the optimal flow rate was 0.0342 kg/s with NO emission concentration of 226.24 mg/Nm^3 and NH_3 slip of 3.43 mg/Nm^3 .

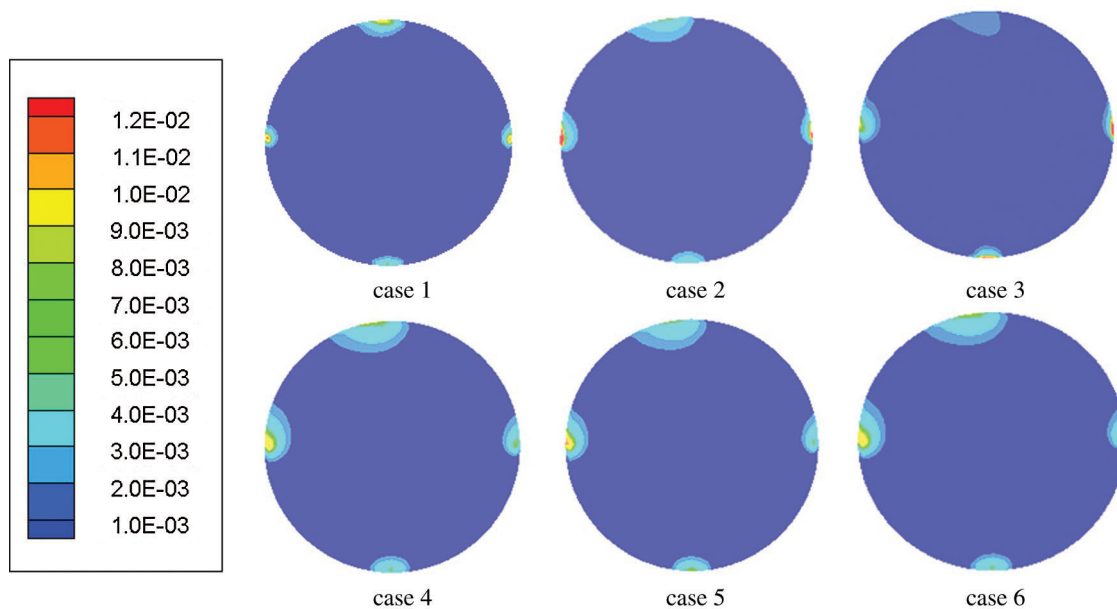


Figure 19: The contours of NH_3 concentration in the precalciner under different flow rates at SNCR-1

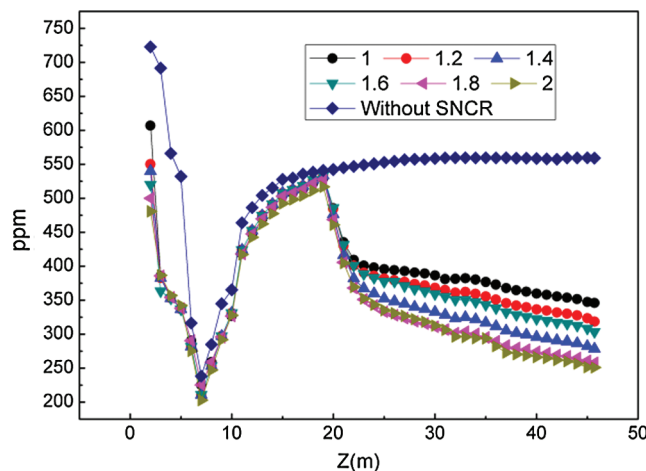


Figure 20: The average NO concentration under different flow rates along the z direction

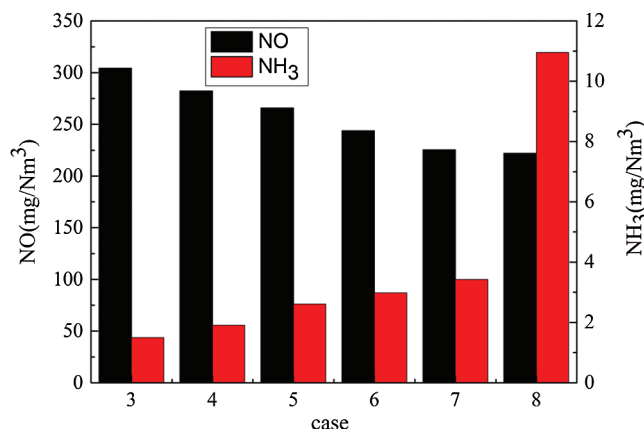


Figure 21: NO and NH₃ concentration at the outlet under different flow rates

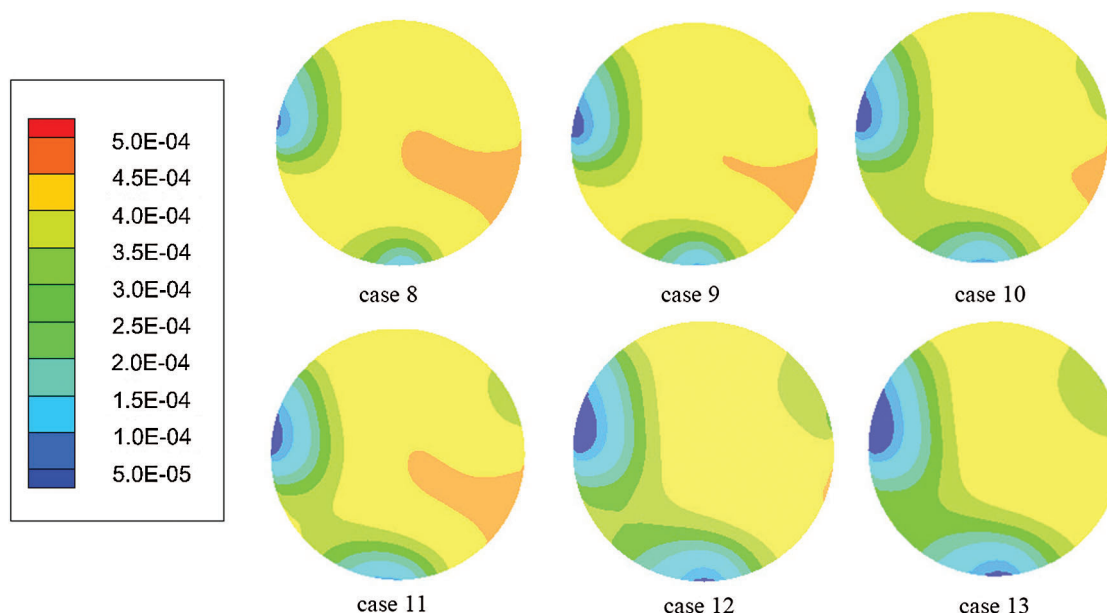


Figure 22: The contours of NO concentration in the precalciner under fixed ratio injection at SNCR-3

3.4.3 Effects of Stratified Injection under Different Flow Rates

The contours of NO concentration and NH₃ concentration under the ratio of 7:2:1 are displayed in Figs. 22 and 23, respectively. Moreover, NO and NH₃ concentration at the outlet under different condition are shown in Figs. 24 and 25.

Compared to the effect of injection height and flow rates, both NO and NH₃ concentrations at SNCR-3 were lower by fixed ratio injection, which could attribute to the effect of stratified injection, the former was because large amounts of NO was reduced at SNCR-1 and SNCR-2, resulting in the lower NO concentration at SNCR-3, the latter was because the aqueous urea solution was not injected into SNCR-3 completely, NH₃ produced by urea decomposition was consumed by reacting with NO between 20 m and 30 m, leading to a lower NH₃ concentration at SNCR-3. Moreover, the distribution of NO under stratified injection was more nonuniform in Fig. 22 compared to Figs. 14 and 18. This is also because when $z = 30$ m, the temperature distribution (Fig. 9) was more uneven, resulting in different denitration efficiency, which further led to more uneven NO distribution at SNCR-3.

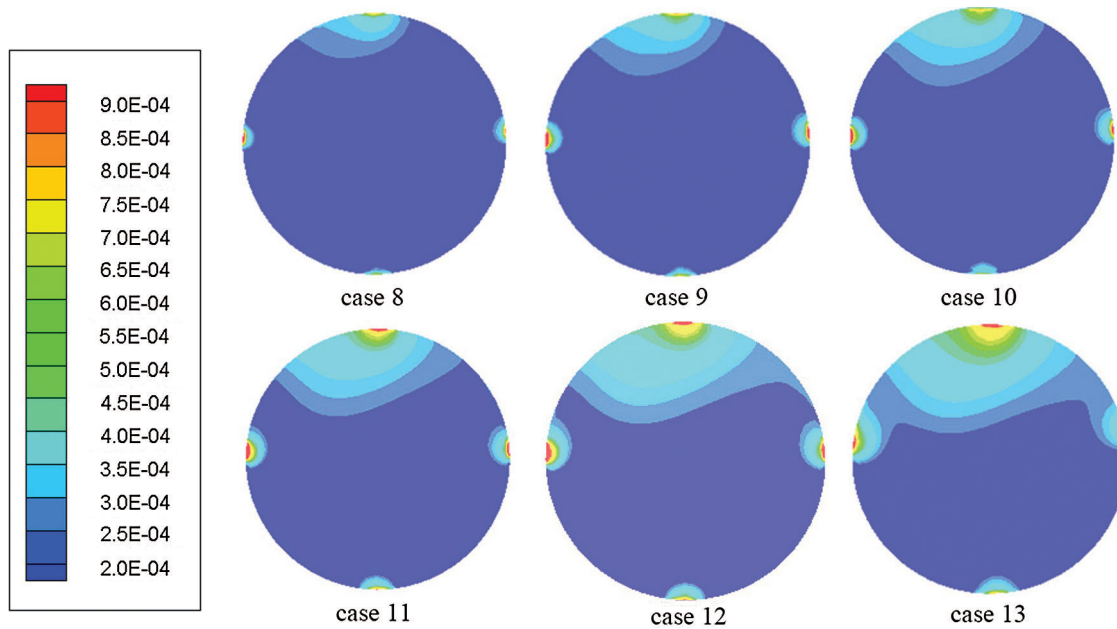


Figure 23: The contours of NH_3 concentration in the precalciner under fixed ratio injection at SNCR-3

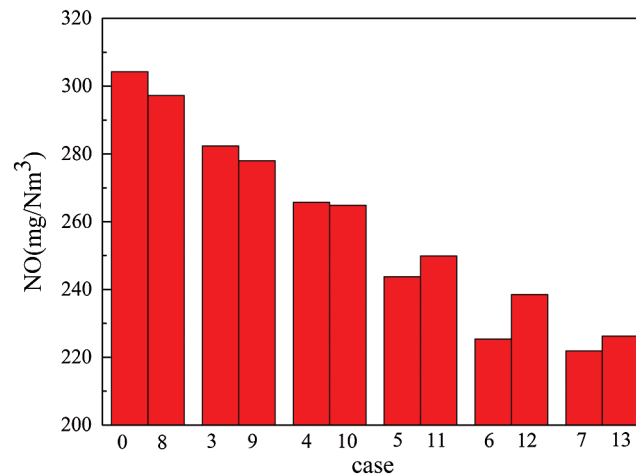


Figure 24: NO concentration at the outlet under different condition

From Figs. 24 and 25, it can be observed that NO concentrations at the outlet were $226.24 \text{ mg}/\text{Nm}^3 \sim 297.27 \text{ mg}/\text{Nm}^3$, the reduction efficiency was 39.36% to 53.85%, and NH_3 slip was $4.67 \text{ mg}/\text{Nm}^3 \sim 10.59 \text{ mg}/\text{Nm}^3$. Moreover, NO concentrations at the outlet in case 8, case 9 and case 10 were lower than that at the outlet in case 0, case 3 and case 4, respectively, which could be attributed to proper stratified injection could slow down the competition of SNCR reaction [37]. However, NO concentrations at the outlet in case 11, case 12 and case 13 were higher than that at the outlet in case 5, case 6 and case 7. This may be because although stratified injection could reduce the competition of SNCR reaction, with the increase of aqueous urea solution at SNCR-3, the shorter reaction time played a more important role in SNCR reaction. Therefore, the flow rate of aqueous urea solution at SNCR-3 had a strong effect on the slip of unreacted NO , and decreasing the flow rate of that at SNCR-3 was conducive to reducing NO_x emission. What's more, NH_3 slips of case 8, case 9, case 10, case 11 and case 12 were much higher than

that of case 0, case 3, case 4, case 5 and case 6, respectively, which could be attribute to the residence time of NH_3 was shorter at SNCR-3 and the reduction of NO was incomplete, leading to higher NH_3 slip. Therefore, the flow rate of aqueous urea solution at SNCR-3 had an adverse effect on the slip of NH_3 , and the greater the flow rate, the more serious the slip of NH_3 . Besides, NH_3 slip at the outlet in case 7 and case 13 was similar, as mentioned above, when $\text{NSR} > 1.8$, the effect of flow rate on the reduction efficiency of NO was small, meaning that NH_3 slip was serious.

In a word, the effects of stratified injection and different flow rates on NOx removal efficiency were different, When the flow rate of stratified injection was 0.019 kg/s, NO concentration at the outlet of the precalciner dropped the most, meanwhile, NH_3 slip met the emission standard. Therefore, the optimal injection flow rate under stratified injection was 0.019 kg/s with NO emission concentration of 297.27 mg/Nm^3 and NH_3 slip of 4.67 mg/Nm^3 , which could play a better optimization role on NO removal efficiency on the basic of the injection flow rate.

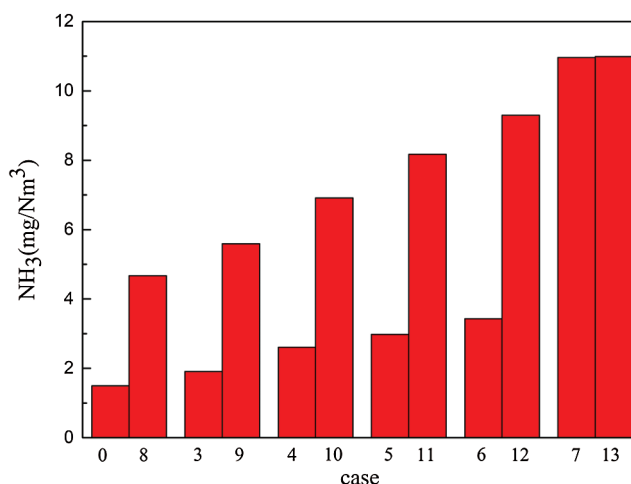


Figure 25: NH_3 concentration at the outlet under different condition

4 Conclusions

In this article, a numerical simulation of the full-scale trinal-sprayed precalciner was enforced to study the transport of gas-solid two-phase flow, combustion characteristics, NOx emission and NH_3 slip in the precalciner. The results showed the flue gas from the rotary kiln formed the recirculation region on both sides of the cone body, which increased the residence time of the solid particles, and facilitated heat exchange between the raw meals and the gas and CaCO_3 decomposition, further, there were high temperature and low temperature zones in the precalciner, the high temperature zone was mainly distributed in the cone of the precalciner and pulverized coal main combustion area, and the low temperature zone was mainly distributed in the middle and upper column section of the precalciner. In addition, the calcium carbonate decomposition was mainly concentrated in the middle and lower column section of the precalciner, and the predicted CaCO_3 decomposing rate was 90.51%, which was in accordance with the actual measured data.

The concentration of nitric oxide was predicted and the NO concentration at the outlet was 559 ppm. Moreover, different injection heights and different injection flow rates had a strong effect on NOx removal efficiency and NH_3 slip. The aqueous urea solution should be injected at SNCR-1 to prolong the reaction time between NH_3 and NO, and injection flow rate had an optimal flow rate but not the higher the better. When the injection flow rate under stratified injection was 0.019 kg/s, which could play a

better optimization role on NO removal efficiency on the basis of the injection flow rate. In consideration of cost effective, A stratified injection with an injection flow rate of 0.019 kg/s and an injection height of 20 m, 25 m and 30 m was suggested as a compromise of a satisfactory NO_x reduction rate and reasonable NH₃ slip. Under this condition, numerical simulation result showed that NO_x concentration at the outlet of precalciner was 297.27 mg/Nm³ and NH₃ slip was 4.67 mg/Nm³, meeting emission standard.

Funding Statement: This work was supported by the general institute of building materials research of china (No. 2017YFC0210801) and the Priority Academic Program Development of Jiangsu Higher Education Institutions (PAPD).

Conflicts of Interest: The authors declare that they have no conflicts of interest to report regarding the present study.

References

1. Hashem, F. S., Razek, T. A., Mashout, H. A. (2019). Rubber and plastic wastes as alternative refused fuel in cement industry. *Construction and Building Materials*, 212, 275–282. DOI 10.1016/j.conbuildmat.2019.03.316.
2. Hossain, M. U., Poon, C. S., Kwong, W. M. Y., Khine, A. (2019). Techno-environmental feasibility of wood waste derived fuel for cement production. *Journal of Cleaner Production*, 230, 663–671. DOI 10.1016/j.jclepro.2019.05.132.
3. Wei, X., Xu, J., Jia, L., Li, H., Bo, C. et al. (2014). The utilization of lime-dried sludge as resource for producing cement. *Journal of Cleaner Production*, 83, 286–293. DOI 10.1016/j.jclepro.2014.07.070.
4. Ping, L., Zhao, G., Lin, X., Gu, Y., Xu, J. (2020). Feasibility and carbon footprint analysis of lime-dried sludge for cement production. *Sustainability*, 12(6), 2500. DOI 10.3390/su12062500.
5. Xu, Y., Zhang, Y., Wang, J., Yuan, J. (2013). Application of CFD in the optimal design of a SCR-DeNO_x system for a 300 MW coal-fired power plant. *Computers and Chemical Engineering*, 49, 50–60. DOI 10.1016/j.compchemeng.2012.09.014.
6. Vignesh, R., Ashok, B. (2020). Critical interpretative review on current outlook and prospects of selective catalytic reduction system for De-NO_x strategy in compression ignition engine. *Fuel*, 276, 117996. DOI 10.1016/j.fuel.2020.117996.
7. Fan, W., Li, Y., Guo, Q., Chen, C., Wang, Y. (2017). Coal-nitrogen release and NO_x evolution in the oxidant-staged combustion of coal. *Energy*, 125, 417–426. DOI 10.1016/j.energy.2017.02.130.
8. Kang, M. S., Jeong, H. J., Massoudi, F. M. (2017). Effect of staged combustion on low NO_x emission from an industrial-scale fuel oil combustor in South Korea. *Fuel*, 210, 282–289. DOI 10.1016/j.fuel.2017.08.065.
9. Fan, W., Zhu, T., Sun, Y. (2014). Effects of gas compositions on NO_x reduction by selective non-catalytic reduction with ammonia in a simulated cement precalciner atmosphere. *Chemosphere*, 113, 182–187. DOI 10.1016/j.chemosphere.2014.05.034.
10. Li, S., Ge, Y., Wei, X. (2018). Experiment on NO_x reduction by advanced reburning in cement precalciner. *Fuel*, 224, 235–240. DOI 10.1016/j.fuel.2018.03.039.
11. Hu, Z., Jiang, E., Ma, X. (2019). Numerical simulation on operating parameters of SNCR process in a municipal solid waste incinerator. *Fuel*, 245, 160–173. DOI 10.1016/j.fuel.2019.02.071.
12. Cheng, G., Zhang, C. (2018). Desulfurization and denitrification technologies of coal-fired flue gas. *Polish Journal of Environmental Studies*, 27(2), 481–490. DOI 10.15244/pjoes/75959.
13. Li, Y., Fan, W. (2019). Effect of char gasification on NO_x formation process in the deep air-staged combustion in a 20 kW down flame furnace. *Applied Energy*, 164, 258–267. DOI 10.1016/j.apenergy.2015.11.048.
14. Li, S., Wei, X., Guo, X. (2012). Effect of H₂O vapor on NO reduction by CO: experimental and kinetic modeling study. *Energy & Fuels*, 26(7), 4277–4283. DOI 10.1021/ef300580y.
15. Wu, H., Ren, Q., Cai, J. (2019). Research on the dynamic process of NO heterogeneous and homogeneous reduction with cement raw meal in vertical tubular reactor. *Journal of the Energy Institute*, 93(3), 878–888. DOI 10.1016/j.joei.2019.07.011.

16. Fu, S., Song, Q., Tang, J. (2014). Effect of CaO on the selective non-catalytic reduction deNO process: experimental and kinetic study. *Chemical Engineering Journal*, 249, 252–259. DOI 10.1016/j.cej.2014.03.102.
17. Fu, S., Song, Q., Yao, Q. (2015). Experimental and kinetic study on the influence of CaO on the $N_2O + NH_3 + O_2$ system. *Energy & Fuels*, 29(3), 1905–1912. DOI 10.1021/ef502512f.
18. Fu, S., Song, Q., Yao, Q. (2015). Study on the catalysis of $CaCO_3$ in the SNCR deNO_x process for cement kilns. *Chemical Engineering Journal*, 262, 9–17. DOI 10.1016/j.cej.2014.09.048.
19. Xie, J., Mei, S. (2007). Numerical simulation of gas-solid flow in SLC-S precalciner by adding a raw meal inlet. *Kuei Suan Jen Hsueh Pao/Journal of the Chinese Ceramic Society*, 35, 1382–1388.
20. Huang, L., Lu, J., Xia, F., Li, W. (2006). 3-D mathematical modeling of an in-line swirl-spray precalciner. *Chemical Engineering and Processing: Process Intensification*, 45(3), 204–213. DOI 10.1016/j.cep.2005.09.001.
21. Fidaros, D. K., Baxevanou, C. A., Dritselis, C. D. (2007). Numerical modelling of flow and transport processes in a calciner for cement production. *Powder Technology*, 171(2), 81–95. DOI 10.1016/j.powtec.2006.09.011.
22. Hu, Z., Ma, X., Chen, Y., Liao, Y., Wu, J. et al. (2015). Co-combustion of coal with printing and dyeing sludge: numerical simulation of the process and related NO_x emissions. *Fuel*, 139, 606–613. DOI 10.1016/j.fuel.2014.09.047.
23. Xia, Z., Li, J., Wu, T., Chen, C., Zhang, X. (2014). CFD simulation of MSW combustion and SNCR in a commercial incinerator. *Waste Management*, 34(9), 1609–1618. DOI 10.1016/j.wasman.2014.04.015.
24. Huang, L., Lu, J., Hu, Z., Wang, S. (2006). Numerical simulation and optimization of NO emissions in a precalciner. *Energy & Fuels*, 20(1), 164–171. DOI 10.1021/ef0502857.
25. Sun, Y., Fan, W., Zhu, T., Hong, X. (2017). Effect of CaO on NO_x reduction by selective non-catalytic reduction under variable gas compositions in a simulated cement precalciner atmosphere. *International Journal of Environmental Research and Public Health*, 14(12), 1474.
26. Mikulčić, H., Vujanović, M., Fidaros, D. K., Priesching, P., Minić, I. et al. (2012). The application of CFD modelling to support the reduction of CO₂ emissions in cement industry. *Energy*, 45(1), 464–473. DOI 10.1016/j.energy.2012.04.030.
27. An, H., Yang, W. M., Li, J., Zhou, D. Z. (2015). Modeling analysis of urea direct injection on the NO_x emission reduction of biodiesel fueled diesel engines. *Energy Conversion and Management*, 101, 442–451. DOI 10.1016/j.enconman.2015.06.008.
28. Modliński, N. (2015). Numerical simulation of SNCR (selective non-catalytic reduction) process in coal fired grate boiler. *Energy*, 92, 67–76. DOI 10.1016/j.energy.2015.03.124.
29. Anderson, J. (2002). *Computational fluid dynamics*. China: Tsinghua University Press.
30. Shih, T. H., Liou, W. W., Shabbir, A., Yang, Z., Jiang, Z. (1995). A new κ - ϵ eddy viscosity model for high reynolds number turbulent flows. *Computers & Fluids*, 24(3), 227–238. DOI 10.1016/0045-7930(94)00032-T.
31. Sazhin, S. S., Sazhina, E. M. (1996). The P-1 model for thermal radiation transfer: advantages and limitations. *Fuel*, 75(3), 289–294. DOI 10.1016/0016-2361(95)00269-3.
32. Gómez, M. A., Porteiro, J., Míguez, J. L. (2016). Numerical simulation of the combustion process of a pellet-drop-feed boiler. *Fuel*, 184, 987–999.
33. Fluent Inc. User's Guide. (2006).
34. Branco, J., Coelho, P. J., Costa, M. (2016). Experimental and numerical investigation of turbulent diffusion flames in a laboratory combustor with a slot burner. *Fuel*, 175, 182–190. DOI 10.1016/j.fuel.2016.02.046.
35. Miller, R. S., Harstad, K., Bellan, J. (1998). Evaluation of equilibrium and non-equilibrium evaporation models for many-droplet gas-liquid flow simulations. *International Journal of Multiphase Flow*, 24(6), 1025–1055. DOI 10.1016/S0301-9322(98)00028-7.
36. Mei, S., Xie, J., Chen, X., He, F., Yang, H. et al. (2017). Numerical simulation of the complex thermal processes in a vortexing precalciner. *Applied Thermal Engineering*, 125, 652–661. DOI 10.1016/j.applthermaleng.2017.07.041.
37. Valera, M. A., Marsh, R., Runyon, J., Pugh, D., Beasley, P. (2017). Ammonia–methane combustion in tangential swirl burners for gas turbine power generation. *Applied Energy*, 185, 1362–1371. DOI 10.1016/j.apenergy.2016.02.073.